Photodissociation of H_2O and D_2O in $\tilde{B}$, $\tilde{C}$, and $\tilde{D}$ States (134−119 nm). Comparison between Experiment and ab Initio Calculations

J. H. Fillion,*,†,‡ R. van Harrevelt,§ J. Ruiz,⊥ M. Castillejo,▽ A. H. Zanganeh,† J. L. Lemaire,†,‡ M. C. van Hemert,§ and F. Rostas†

Observatoire de Paris-Meudon, DAMAp et UMR 8588 du CNRS, 92195 Meudon Cedex, France, Université de Cergy-Pontoise, 95806 Cergy Cedex, France, Leids Institut voor Chemisch Onderzoek, Gorlaeus Laboratoria, Universiteit Leiden, Postbus 9502, 2300 RA Leiden, The Netherlands, Departamento de Física Aplicada, Facultad de Ciencias, Universidad de Málaga, Málaga, Spain, and Instituto de Química Física "Rocasolano", CSIC, Serrano 119, 28006 Madrid, Spain

Received: August 7, 2001; In Final Form: October 9, 2001

Rotational and vibrational state distributions have been measured for the OH/OD($A^2\Sigma^+$) fragment produced by the photodissociation of H_2O/D_2O at a set of wavelengths in the 133−119 nm range that lead to excitation of the $\tilde{B}(^1A_1)$ state, either directly or through particular absorption features of the $\tilde{C}^1B_1 \leftarrow \tilde{X}^1A_1$ and $\tilde{D}^1A_1 \leftarrow \tilde{X}^1A_1$ Rydberg transitions. The experimental distributions are obtained from the $A^2\Sigma^+-X^2\Pi$ fluorescence spectra using a truncated single value decomposition method (TSVD). They are compared to distributions calculated in a complete three-dimensional quantum mechanical treatment by using two sets of diabatic potential energy surfaces obtained by Dobbyn and Knowles (DK) and by van Harrevelt and van Hemert (Leiden). The measured vibrational branching ratios seem to be better accounted for by the former and the rotational distributions by the latter. However, a more detailed analysis indicates that the DK surface would presumably account for the experiment if the room-temperature rotational distribution of the parent water molecule were introduced in the calculation. The experimental results are therefore interpreted as a confirmation of the more direct and shorter-lived trajectories favored by the DK surface.

I. Introduction

Photodissociation of water in the vacuum ultraviolet (VUV) has attracted much attention from both experimental and theoretical sides over the last two decades.[1] Advances in experimental techniques, for both initial excitation and fragment detection, together with progress in ab initio quantum theory calculations, have contributed to the understanding of the processes involved. Monitoring of the OH(A) product fluorescence following VUV excitation of the parent molecule is a powerful tool for probing details of the dissociation process especially if, as is the case here, the experiments can be associated with dedicated ab initio calculations. Indeed, the rovibrational energy distribution in the fragment is sensitive to details of the dissociation path and comparison of calculated and measured distributions should be enlightening. The aim of the present study has precisely been to provide such comparison over the whole range of excitation energies in which the photodissociation proceeds via the $\tilde{B}(^1A_1)$ state. In particular, it is hoped that information will be obtained on the longer-lived indirect trajectories that appear in the calculations.

The electronic absorption spectrum of water (Figure 1) is associated with Rydberg states of different geometries.[2−4] The excitation of an electron out of the nonbonding $1b_1$ orbital to a Rydberg orbital results in Rydberg states of bent equilibrium geometry converging to the first ionization potential (IP). Excitation of electrons from the inner $3a_1$ orbital gives rise to linear Rydberg states converging to a higher IP. The coupling of states with linear and bent geometries is the reason for the complexity of the observed photochemistry of the molecule. The dissociative first excited state $3s \leftarrow 1b_1$ $\tilde{A}(^1B_1)$ is responsible for the first broad absorption continuum extending below 190 nm with maximum at 167 and 166 nm for H_2O and D_2O, respectively. At higher energy lies the $\tilde{B}(^1A_1)$ state that results from strongly interacting $3s \leftarrow 3a_1$ and $3p_x \leftarrow 1b_1$

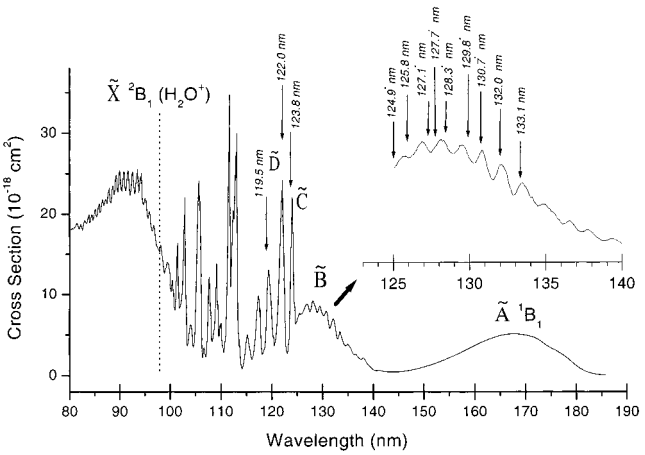

Figure 1. Absorption spectrum of H_2O at room temperature (adapted from refs 3 and 44). The positions of the photolysis excitation wavelengths used in this work are indicated by arrows (see also Table 2). The wavelengths studied earlier with VUV laser excitation[30] are marked by an asterisk.

* To whom correspondence should be addressed. E-mail: jean-hugues.fillion@obspm.fr.
† Observatoire de Paris-Meudon.
‡ Université de Cergy-Pontoise.
§ Universiteit Leiden.
⊥ Universidad de Málaga.
▽ Instituto de Química Física "Rocasolano".

10.1021/jp013032x CCC: $20.00
Published on Web 12/01/2001

excitations.[5] The $\tilde{B}(^1A_1) \leftarrow \tilde{X}(^1A_1)$ transition gives rise to the second absorption continuum with its maximum at 128 and 127 nm for H_2O and D_2O, respectively. Superimposed on the continuum, there exists an oscillatory structure, less pronounced for D_2O than for H_2O.

The origin of this structure has been the subject of discussions. Weide et al.[5] have argued that it is associated to resonant trajectories that comprise both bending and stretching motions. More recently, van Harrevelt and van Hemert[6,7] have shown that resonances on the $\tilde{B}(^1A_1)$ state exist with a rather long lifetime even at high energies. The $\tilde{B}(^1A_1)$ state is strongly predissociated by a conical intersection with the ground state $\tilde{X}(^1A_1)$ surface. Renner−Teller coupling to the dissociative $\tilde{A}(^1B_1)$ state also contributes to the predissociation.[8,9]

Transitions $3p_z \leftarrow 1b_1$ ($\tilde{C}^1B_1 \leftarrow \tilde{X}^1A_1$)[10] and $3s \leftarrow 3a_1/3p_x \leftarrow 1b_1$ ($\tilde{D}^1A_1 \leftarrow \tilde{X}^1A_1$)[10,11] have their electronic origins around 124 and 121.9 nm, respectively. The $\tilde{C}^1B_1$ state presents a *J*-dependent predissociation that is attributed to a heterogeneous predissociation pathway via rotational coupling to the $\tilde{B}(^1A_1)$ surface.[3,12] All of the levels of the $\tilde{C}$ state are also affected by a purely electronic coupling, presumably to the lower-lying $\tilde{A}^1B_1$ state.[12] This pathway, contrary to the $\tilde{B}$ state pathway does not lead to OH(A) fluorescent fragments. The $\tilde{D}^1A_1$ state shows no rotational structure because of the strong predissociation caused by an avoided crossing with the $\tilde{B}(^1A_1)$ state at bent geometries.[6,13] At higher energies, in the 119−113 nm absorption region, a number of states showing a resolvable rotational structure similar to that of the $\tilde{C}^1B_1$ state have been identified by multiphoton ionization (MPI) techniques.[14]

Excitation at wavelengths below 132 nm gives rise to a rich photochemistry. Four possible dissociation channels are open in this energy region: (i) $OH(X^2\Pi) + H$, (ii) $OH(A^2\Sigma^+) + H$, (iii) $O(^3P/^1D/^1S) + H_2$, and (iv) $O(^3P) + 2H$. A direct electronically adiabatic route for photodissociation via the $\tilde{B}(^1A_1)$ state gives $OH(A^2\Sigma^+) + H$ as final products. This route is also open when the molecule is excited in the $\tilde{C}^1B_1$ and $\tilde{D}^1A_1$ states through coupling between these states and the $\tilde{B}(^1A_1)$ continuum.[16] The route leading to $OH(A^2\Sigma^+)$ fragments accounts for approximately 14% of the photodissociation events.[9] Various authors have measured the spontaneous $OH/OD(A^2\Sigma^+)$ fluorescence that follows photolysis in the continuum region of the $\tilde{B}(^1A_1) \leftarrow \tilde{X}(^1A_1)$ band, at wavelengths longer than 128 nm, at the absorption maximum, and in the region of shorter wavelengths where contributions of the $\tilde{C}^1B_1 \leftarrow \tilde{X}^1A_1$ and $\tilde{D}^1A_1 \leftarrow \tilde{X}^1A_1$ Rydberg transitions dominate the spectrum. Carrington[17] measured more than 20 years ago the rotational distribution resulting from the excitation at 130.2 and 121.6 nm and the vibrational branching between states $v' = 0, 1, 2$. Okabe[18] reported the vibrational and rotational distributions of the $OH(A^2\Sigma^+)$ fragment from H_2O photolysis at 123.6 nm. Gedanken[19] measured the vibrational and rotational distributions of $OD(A^2\Sigma^+)$ from D_2O photolysis at 130.2, 123.6, and 121.6 nm. The vibrational distribution in this fragment following two-photon excitation at 248 nm was also determined.[20] Rotationally resolved photofragment alignment and population distributions were obtained[21] for $OH(A^2\Sigma^+, v' = 0)$ fragments generated through photodissociation of H_2O by atomic resonance radiation at 130.4, 129.5, 123.6, and 121.6 nm. The rotational distribution of the $v' = 0$ state has been measured at dissociation wavelengths of 124[22] and 133 nm[23−25] by excitation through two-photon absorption of the parent molecule. Simons and coworkers[16,21,22] attempted to establish a correlation between the observed rovibrational $OH(A^2\Sigma^+)$ distributions and the initially prepared parent molecular state. $OH(A^2\Sigma^+, v' = 0)$ rotational distributions were obtained following population of individually selected rovibrational levels in the origin band of the $\tilde{C}(^1B_1) \leftarrow \tilde{X}^1A_1$ system in H_2O and D_2O. Differences in the rotational distributions and on product alignment were rationalized in terms of the selective participation in the excitation of the underlying $\tilde{B}(^1A_1) \leftarrow \tilde{X}^1A_1$ continuum. More recently, Harich et al.[26] have measured the OH(A) product state distribution and anisotropy and its dependence with parent rotational excitation, as resulting from H Lyman α excitation using the high-resolution H atom Rydberg "tagging" technique.

The above results, together with the existing theoretical calculations,[27−29] have provided a general picture of the energy disposal on the $OH/OD(A^2\Sigma^+)$ fragments, which are formed vibrationally cold with a highly inverted rotational distribution having a maximum near the highest rotational level, N'_{max}, energetically accessible at the excitation wavelength used. The extremely high degree of rotational excitation has been attributed[27] to the large change in bond angle in going from the ground to the linear dissociative $\tilde{B}$ potential surface. However, these results did not constitute a systematic study of the rovibrational population distribution of $OH/OD(A^2\Sigma^+)$ as a function of the excitation energy and its correlation with the participation of direct or indirect trajectories leading to the dissociation on the $\tilde{B}(^1A_1)$ surface. This is due to the fact that the number of photodissociation wavelengths explored is limited and does not cover systematically the features of the absorption spectrum. Other deficiencies are the poor knowledge of vibrational branching ratios,[18−20] lack of agreement with the available calculations,[28] and the variety of spectral analysis methods used to obtain the rotational population distributions.

In a previous work,[30] some of us have presented a coherent determination of the rotational and vibrational distributions in the $OH/OD(A^2\Sigma^+)$ fragments produced by VUV photodissociation of H_2O/D_2O as a function of excitation energy. VUV laser radiation was used to photodissociate the parent molecules at different wavelengths chosen in the range between 132 and 124 nm so as to excite exclusively the $\tilde{B}(^1A_1)$ and not the $\tilde{C}(^1B_1)$ state. A significant contribution of OH in higher vibrational levels was observed. We showed that the general trend of the experimental results is rather well reproduced by a phase space theory calculation and by ab initio calculations reported by van Hemert and van Harrevelt.[6,7]

The general objective of the present work is to extend the above study by selecting a set of photolysis wavelengths that correspond to excitation in the $\tilde{B}(^1A_1) \leftarrow \tilde{X}^1A_1$ continuum and in specific absorption features of the $\tilde{C}^1B_1 \leftarrow \tilde{X}^1A_1$ and $\tilde{D}^1A_1 \leftarrow \tilde{X}^1A_1$ Rydberg transitions (see Figure 1). This project has been carried out by using synchrotron radiation at six different wavelengths (seven for D_2O) in the range between 134 and 119 nm. Two of them (three for D_2O), namely, 133.1 and 132.0 (133.0, 131.6, and 129.0 for D_2O), coincide with subsidiary maxima on the long-wavelength side of the $\tilde{B}-\tilde{X}$ continuum. The three shorter wavelengths, 123.8, 122.0, and 119.5 (123.8, 121.9, and 120.3 for D_2O), correspond to excitation in the $\tilde{C}(000)$, $\tilde{D}(000) + \tilde{C}(010)$, and $\tilde{D}(010) + \tilde{C}(100)$ (in the $\tilde{C}(000)$, $\tilde{D}(000)$, and $\tilde{D}(010) + \tilde{C}(100)$ for D_2O) absorption features, respectively (see Table 1).

As in previous work,[30] the rovibrational population distributions of the OH(OD) fragment were obtained by analysis of the spontaneous $OH/OD(A^2\Sigma^+ \rightarrow X^2\Pi)$ fluorescence spectra using a procedure based on a truncated singular value decomposition (TSVD) method.[31] In the present work, the distributions were corrected for the effect of predissociation that affects high v' and N' levels. Indeed, the excitation energies used here are

TABLE 1: H_2O/D_2O Levels Excited at the Shorter Photolysis Wavelengths of This Work

λ (nm)	H_2O	D_2O
123.8	$\tilde{C}(000)$	$\tilde{C}(000)$
122.0	$\tilde{D}(000) + \tilde{C}(010)$	
121.9		$\tilde{D}(000)$
120.3		$\tilde{C}(100) + \tilde{D}(010)$
119.5	$\tilde{C}(100) + \tilde{D}(010)$	

often higher than in our previous work (up to 1.2 eV excess energy). Thus, a larger proportion of high v' and N'' levels of OH(OD) become accessible and require such a correction.

The experimental results are compared with accurate three-dimensional quantum mechanical calculations. The calculations assume that only the $\tilde{B}$ and $\tilde{X}$ states are involved in the dissociation dynamics. As seen below, the present work seems to support this hypothesis. The electronically nonadiabatic coupling between the $\tilde{B}$ and $\tilde{X}$ states is included in the theoretical treatment. Two sets of coupled diabatic potential energy surfaces (PES) are used: the Leiden surfaces[6] and the recent Dobbyn−Knowles (DK) surfaces.[37]

II. Experiments

Experiments were performed on the Super-ACO synchrotron ring at Orsay using the SA63 beam line equipped with a 3 m grazing incidence concave grating monochromator. They were conducted with a 2200 lines/mm grating and 2 mm wide slits that provided an excitation line width of 0.4 nm. VUV light emerging from the monochromator is refocused at the center of the photodissociation chamber by a toroidal mirror. The photodissociation chamber and the fluorescence detection system have been described in detail in a previous paper,[30] and only a brief description will be given here. The chamber is a stainless steel cube of 30 cm per side that can be pumped down to 10^{-6} Torr. It is separated from the beam line by a lithium fluoride window. At the exit of the chamber, the VUV light beam impinges on a window coated on its inner side with a thin layer of sodium salicylate. Visible light emitted by the coating upon VUV illumination is viewed by a photomultiplier. Wavelength calibration and intensity monitoring of the VUV light beam are obtained by recording the absorption spectrum of the A−X transition of the CO molecule[32] (or, with less accuracy, with the absorption spectrum of H_2O/D_2O itself).

H_2O/D_2O vapor was continuously flowing through the chamber during the experiments. The water pressure was kept constant by an electronic regulator acting on a needle valve controlling the gas flow. The experiments were all performed at a pressure of 0.15 Torr as measured by a capacitance manometer. This pressure was chosen because it maximizes the fluorescence signal intensity in view of the quenching of the excited OH radical by collisions with parent H_2O molecules. Distilled H_2O vapor (99.99% purity) and D_2O (CEA Eurisо-Top 99.95% purity) were used in the experiments, both after some outgassing cycles.

Spontaneous OH/OD($A^2\Sigma^+$) fluorescence was observed perpendicularly to the VUV beam through a quartz window on the upper side of the cell and imaged after reflection on a flat mirror onto the entrance slit of a Jobin−Yvon−Spex Triax 320 (32 cm, f/4.1) monochromator by a fused silica lens ($f = 100$ mm, 5 cm diameter). Most of the experiments were carried out with a 1200 lines/mm grating at a dispersion of 3 nm/mm. By using an entrance slit of 150 μm width and effective height of 5 mm, the achieved resolution was 0.3 nm. A few control experiments were done with a 2400 lines/mm grating at a resolution of 0.15 nm using a 150 μm slit. The fluorescence light was detected with an intensified charge coupled device (CCD) camera (ANDOR/Oriel DH520L) equipped with a 1024 × 256 pixels (26 × 26 μm^2) CCD from EEV and a three-stage cooler (usually set at −33 °C). The useful area of the CCD is in fact reduced to 850 × 256 pixels because of the MCP intensifier diameter of 25 mm. This covers a spectral range of 65 nm allowing us to record simultaneously the $\Delta v = -1$ and $\Delta v = 0$ progressions for OH and the $\Delta v = -2$, $\Delta v = -1$, and $\Delta v = 0$ progressions for OD.

In this paper, results obtained using synchrotron VUV excitation will be presented together with previous measurements using VUV laser excitation.[30] The main difference between the two experiments lies in the duration and the repetition rate of the excitation events, which implies some modifications of the detection scheme. In the case of laser excitation with 12 ns light pulses at 10 Hz, the intensifier placed in front of the CCD detector was used as a fast electronic shutter, which was opened a few nanoseconds after the end of the laser pulse and closed a few hundred nanoseconds later, when the fluorescence had decayed. This allowed rejection of the short pulse of stray light originating from the primary laser beams used to generate the VUV radiation as well as the background, which continuously accumulates on the CCD detector. The latter is due essentially to the dark current of the intensifier photocathode and to stray light. Suppressing the acquisition in the time interval between pulses rejects about 99% of the continuous background.

In the present experiment, the synchrotron light beam may be considered as a continuous source. Indeed, the synchrotron light is delivered in pulses of 200 ps at intervals of either 10 or 120 ns. Each of these pulses generates a fluorescence pulse of about 200 ns duration so that the fluorescence light is essentially continuous. Although the strong stray light associated with the pulsed laser excitation is no longer present, it is now impossible to eliminate the unwanted continuous dark current background by time discrimination. This contribution can be eliminated by subtraction of a reference background spectrum recorded while the synchrotron beam is turned off.

The final spectra are obtained by co-addition of 1000−4000 individual spectra exposed during 1 s each and corrected by subtracting an equal number of background spectra recorded during the same time. The elemental exposure time is chosen to allow recording correctly the signal plus background without reaching the saturation level of the CCD. Another difference between our synchrotron and laser experiments concerns the excitation line width. The spectral brightness of the present synchrotron source is considerably lower than that of the laser used in our previous experiments.[30] Therefore, to obtain similar signal levels, the synchrotron excitation had to be performed with a 200 times broader spectral band (i.e., 0.4 nm instead of 0.002 nm). Following this procedure and notwithstanding the lower brightness of the synchrotron light source, it is possible to obtain a signal/noise ratio similar to that obtained in the VUV laser excitation experiments at the expense of a considerably larger excitation bandwidth.

III. Details of the Quantum Mechanical Calculations

The theoretical calculation techniques used in this paper are the same as those described in ref 7. The theory is based on papers of Balint-Kurti[33,34] and Petrongolo.[35] Briefly, we use a time-dependent method in which initial wave packets are created on the $\tilde{B}$ state surface. From the time dependence of the propagated wave packets, rovibrational product state distributions can be extracted.

In the present calculations, we only consider excitation into the dissociative $\tilde{B}$ state. We assume that OH(A) rovibrational distributions resulting from excitation into a quasi-bound vibrational level of the $\tilde{C}$ or $\tilde{D}$ state are close to those corresponding to a direct excitation into the $\tilde{B}$ state. This assumption is justified because the equilibrium geometries of the $\tilde{C}$ and $\tilde{D}$ states are close to that of the ground state. The region where the dynamics on the $\tilde{B}$ surface starts is therefore similar for direct excitation into the $\tilde{B}$ state and for predissociation of the $\tilde{C}$ and $\tilde{D}$ states. The strong nonadiabatic coupling between the $\tilde{B}$ and $\tilde{X}$ states at the conical intersections in the linear HOH and HHO regions is treated with a diabatic representation of the two coupled electronic states.[7] Two sets of coupled diabatic states are considered in the present calculations: the recent Dobbyn−Knowles (DK) surfaces[36,37] and the earlier Leiden surfaces.[6] An OH1 + H2 Jacobi coordinate system has been used in the dynamical calculations: **r** is the distance between O and H1, and **R** is the distance between the center of mass of the OH1 group and the H2 atom. The internal coordinates are the magnitudes of the two vectors, r and R, and the angle between them, γ. The total wave function is expanded in products of wave packets, dependent on r, R, and γ only, and roto-electronic basis functions $\Theta_{\Omega\Lambda K}$. Ω is the projection of the total angular momentum on the body-fixed z axis, which is parallel to **r**. Λ and K are the projections of the electronic and vibrational angular momenta on the z axis. Λ is 0 for the Σ state and 1 for the Π state.

We consider water molecules in the rotational ground level ($J'' = 0$). After the excitation, the total angular momentum, J, equals 1. For $J = 1$, the total wave function is expanded in five roto-electronic states. The initial wave function contains three nonzero wave packets $(\Omega\Lambda K) = (010)$, (110), and (112). The probabilities for OH/OD(A) fragments, for which $\Lambda = 0$, to be formed in a state with vibrational quantum number v and rotational quantum number N are given by

$$P^{vN} \propto k_{vN}(E)\sum_{\Omega}\sum_{l}\langle l\Omega,N0|J\Omega\rangle^2\frac{2N+1}{2J+1}A_{\Omega}{}^{vlN}(E) \qquad (1)$$

where the summation is over Ω and l, the orbital angular momentum of the hydrogen atom. E is the total energy, $k_{vN}(E)$ is the wavenumber of the OH(A) fragment, and $\langle l\Omega,N0|J\Omega\rangle$ is a Clebsch−Gordan coefficient. The coefficients $A_{\Omega}{}^{vlN}(E)$ are obtained by analyzing the wave function at a cut at $R = R_{asy}$, where R_{asy} is in the asymptotic region (in the present case, $R_{asy} = 8$ b). If $\phi^v(r)$ is the rovibrational wave function of the OH fragment and $P_{l\Omega}(\gamma)$ an associated Legendre polynomial, then

$$A_{\Omega}{}^{vlN}(E) = |\frac{1}{2\pi}\int_{t=0}^{t=\infty}\mathrm{d}t\,\langle P_{l\Omega}(\gamma)\phi^{vN}(r)\delta(R - R_{asy})\Theta_{\Omega 0\Omega}|\,\mathrm{e}^{i(E-H)t}|\Psi^i(r,R,\gamma)\rangle|^2 \qquad (2)$$

where H is the excited-state Hamiltonian operator. In most theoretical calculations reported in the literature, the molecular rotation is neglected both in the ground state and in the excited state. For this planar model, the summation in eq 1 reduces to one single term, with $\Omega = 0$ and $l = N$. Calculations for $J = 1$ are about twice as expensive in computer time as calculations for $J = 0$. However, the correct treatment of the molecular rotation is preferable, because rotational distributions calculated with the $J = 0$ model show strong random oscillations, which are not observed experimentally. When the molecular rotation is treated correctly, the strong random oscillations are washed out, because each v,N resolved partial cross section is a sum of contributions for various Ω and l values. Thus, the rotational distributions are much smoother when the molecular rotation has been correctly taken into account resulting in a much easier comparison with experiment. Note that the experimental results reported in this paper are performed at room temperature, for which rotational states with J up to 10 contribute to the Boltzmann average.

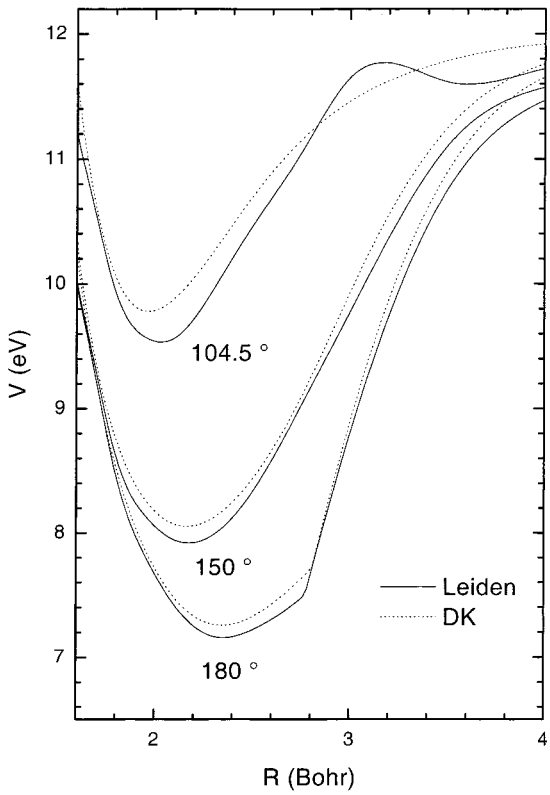

Figure 2. Symmetric stretch potentials for the adiabatic B state: potential energy vs $R = r(\mathrm{OH1}) = r(\mathrm{OH2})$ at three HOH bond angles for the Leiden[6] (solid line) and DK[37] (dotted line) surfaces.

Technical details of the calculations are described in ref 7. Discrete variable representation (DVR) methods have been applied for the internal coordinates r, R, and γ. For r and R, a Fourier grid with a range of 1−10 b is used with 96 and 128 grid points for H_2O and D_2O, respectively. For γ, a DVR based on associated Legendre polynomials has been used with 60 and 90 grid points for H_2O and D_2O, respectively. For the propagation in time, the Lanczos scheme of order 8 is used for a total propagation time of 20 000 atomic units (1 au = 0.024 fs) and a time step of 2 au. Quadratic optical potentials have been used to absorb the outgoing wave function at the ends of the grids.

The rovibrational distributions for the OH/OD(A) fragments calculated using an adiabatic model, in which the coupling with the $\tilde{X}$ state was neglected, are not significantly different from the distributions obtained from the fully coupled calculations. Therefore, the characteristics of the OH/OD(A) rovibrational distributions can be understood by looking at details of the adiabatic $\tilde{B}$ state surface only, although all calculations presented in this paper are obtained from a fully coupled treatment.

The most important difference between the adiabatic Dobbyn−Knowles (DK) and Leiden $\tilde{B}$ surfaces is found in the symmetric stretch potentials, i.e., potential energies as functions of $r_{OH1} = r_{OH2} = r$. In Figure 2, DK and Leiden symmetric stretch potentials for the adiabatic $\tilde{B}$ state are compared for three values of the HOH bond angles (104.5°, 150°, and 180°). For 180° (the linear HOH geometry), both the DK and Leiden

TABLE 2: Comparison of the OH/OD(A) Vibrational Excitation Energies (in cm^{-1}) Calculated with the Leiden[5] and DK[37] Potential Energy Surfaces and Obtained from Spectroscopic Data for OH[39] and for OD[40]

	Leiden	DK	experimental data
OH(A,$v=0$)	0	0	0
OH(A,$v=1$)	2940	3121	2988
OH(A,$v=2$)	5673	6006	5781
OD(A,$v=0$)	0	0	0
OD(A,$v=1$)	2180	2317	2214
OD(A,$v=2$)	4264	4512	4326
OD(A,$v=3$)	6188	6581	6333

symmetric stretch potentials show a kink at $R = 2.8$ b. This is due to the crossing between the Π and Σ states, which becomes an avoided crossing for bent geometries. In the actual calculations, the diabatic representation is used, for which the potential energy surfaces are always smooth.

Figure 2 also shows that the wells in the potential energy curves are deeper for the Leiden surfaces. This may have important the consequences for the photodissociation dynamics: it is expected that the Leiden surface is more favorable to vibrational excitation than the DK surface. Another interesting point is the presence of a barrier at $R = 3.1$ b for the Leiden symmetric stretch potentials for 104.5°, which is absent in the DK potential. The energies at which this barrier occurs are however above the energies relevant to photodissociation at wavelengths considered in this paper, and hence, this barrier is not important for the dynamics. A barrier in the symmetric stretch potential is also found for other excited states[5] and can be explained by the change of the electronic wave function from Rydberg to valence character.

Another important difference is the potential energy of the OH/OD(A) fragment at the OH/OD(A) equilibrium distance, relative to the potential energy of the H_2O/D_2O ground state at the equilibrium geometry, which is taken to be the zero point of the potential energy. The value obtained from experimental data[38] is 9.52 eV, while the calculated values are 9.33 and 9.42 eV for the Leiden and DK calculations, respectively. Therefore, experimental rovibrational distributions at specific photon energies are compared with theoretical results at those photon energies plus 0.19 and 0.10 eV for Leiden and DK, respectively. In Table 2, the vibrational excitation energies for OH/OD(A) are compared with the experimental data described in refs 39 (for OH) and 40 (for OD). The vibrational excitation energies arising from the Leiden potential are too low, while they are too high for the DK potential, the deviation from experiment being largest for the latter. As a consequence, the threshold energies for production of vibrationally excited fragments are slightly lower for the Leiden surface than for the DK surface.

IV. Results

The OH(A, $v' = 0, 1, 2$) rotational distributions were determined for synchrotron radiation excitation of H_2O at 133.1, 132.0, 125.8, 123.8, 122.0, and 119.5 nm. To provide an overall picture of the process and a systematic comparison with the available theoretical results, these data are complemented in the present report by results obtained with VUV laser excitation in our previous work.[30] The situation of these wavelengths on the absorption spectrum of H_2O is shown in Figure 1. For OD, the rotational distributions of the vibrational levels A($v' = 0, 1, 2, 3$) were obtained at the excitation wavelengths of 133.0, 131.6, 129.0, 126.8, 123.8, 121.9, and 120.3 nm. The vapor pressure used during the measurements was 0.15 Torr. A typical OH

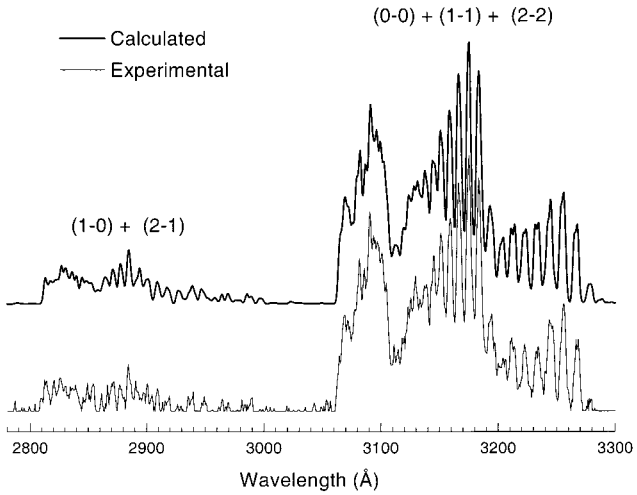

Figure 3. Fluorescence spectra of the OH photofragments produced at 119.5 nm using synchrotron radiation excitation. Water vapor pressure was 0.15 Torr. Temperature was 300 K. The instrumental width is 0.3 nm, and the integration time 1200 s. The synthetic spectrum is calculated using the rotational populations given by the TSVD method and a Gaussian line profile of 0.3 nm half-width.

fluorescence spectrum is shown in Figure 3. It includes the contributions of the $\Delta v = -1$ and $\Delta v = 0$ progressions around 280 and 308 nm, respectively. Because of the strong predissociation discussed below, the intensity of the $\Delta v = -2$ progression in OH is not sufficiently high to be clearly detected above the noise. For OD, the $\Delta v = -1$ progression is displaced toward longer wavelengths (289 nm) and the $\Delta v = -2$ progression appears around 272 nm.

The rovibrational population distributions were obtained by analysis of the fluorescence spectra using a procedure based on a TSVD method, developed by Ruiz and Martín.[31] In this method, the intensity of the spectrum is calculated for a set of wavelengths corresponding to the experimental grid. At each wavelength, the spectrum intensity is obtained as the sum of the contributions of all of the lines. The contribution of each line is determined by the population of the corresponding level, the profile of the line, and the distance of its center from the grid point considered. By setting the calculated intensities equal to the measured ones, one obtains an overdetermined set of equations, in which the level populations are the unknowns. This set of equations is solved by the TSVD procedure. Once the populations have been determined, the same set of equations yields a simulated spectrum, which can directly be compared to the experimental one. The line profile used for these calculations is a Gaussian with 0.3 nm half-width. A discussion of the merits of this technique for the analysis of the population distributions, together with details on the rovibrational line positions and strengths used for the spectrum calculations, has been presented in ref 30.

The populations obtained as described above do not always truly reflect the nascent populations that result from the photodissociation process. Indeed, the high (v', N') levels of OH/OD($A^2\Sigma^+$) are strongly predissociated by the $^4\Sigma^-$, $^2\Sigma^-$, and $^4\Pi$ dissociative states correlating with the ground-state asymptote $O(^3P) + H(^2S)$.[41] These interactions introduce nonradiative decay channels, which compete with the radiative channels and reduce the lifetimes and fluorescence yields of the corresponding levels. Brzozowsky et al.[42] and Bergeman et al.[43] measured the lifetimes τ of the individual F_1 and F_2 rotational sublevels, characterized by values of $j = N \pm 1/2$, of OH($A^2\Sigma^+$, $v' = 0-2$) and OD($A^2\Sigma^+$, $v' = 0-3$), respectively. From these lifetimes,

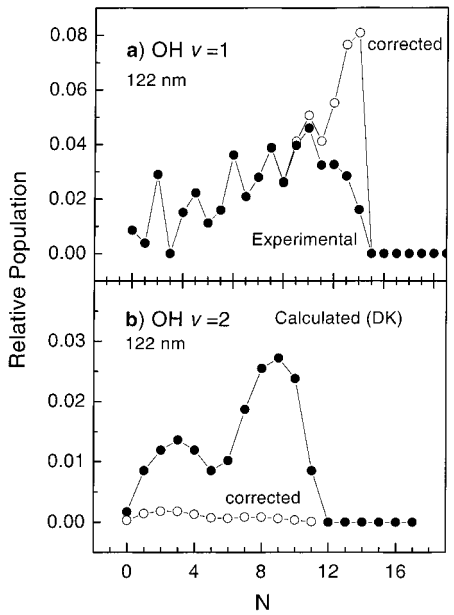

Figure 4. Effect of predissociation on the OH rotational population (photodissociation wavelength = 122 nm). In panel a, the measured OH($A^2\Sigma^+,\upsilon' = 1$) population distribution (full circles) is corrected (open circles) to give the truly nascent distribution (note that the corrected distribution is not normalized). In panel b, the nascent OH($A^2\Sigma^+,\upsilon' = 2$) population distribution calculated on the DK surface (full circles) is corrected to give the measured distribution (open circles).

these authors deduced the predissociation rates, A_{NR}, of the levels lying above the dissociation limit. For OH, levels $\upsilon' = 0$, $N' > 22$, $\upsilon' = 1$, $N' > 13$, and $\upsilon' = 2$, $N' > 0$ are predissociated with non-negligible values of A_{NR}. For OD, the predissociated levels are as follows: $\upsilon' = 0$, $N' > 36$; $\upsilon' = 1$, $N' > 29$; $\upsilon' = 2$, $N' > 15$; $\upsilon' = 3$, $N' > 0$. Yarkony[41] performed a theoretical treatment of the predissociation of the individual rovibronic levels and obtained a set of radiative lifetimes τ_R and total decay rates τ, in good agreement with the available experimental data.[42,43] The effective lifetimes τ are related to the predissociation rates A_{NR} through $1/\tau = 1/\tau_R + A_{NR}$, and thus, the nascent populations, N', can be obtained from the measured populations, N_{TSVD}, by applying the correction: $N' = N_{TSVD}/(1 - \tau A_{NR}) = N_{TSVD}(\tau_R/\tau)$. The rovibrational populations obtained from the measured line intensities by the TSVD method were systematically corrected in this fashion. The calculated values of τ and τ_R[41] were employed to perform this correction. They were preferred to the experimental ones because they provide a more consistent set of correction factors.

The effect of predissociation is negligible on the OH($\upsilon' = 0$) and OD($\upsilon' = 0, 1$) rotational distributions. It has a very small effect on OD($\upsilon' = 2$) and affects significantly the rotational populations of OH($\upsilon' = 1$, $N' > 14$) that result from the photodissociation of H_2O at wavelengths below 123.8 nm. This is illustrated in Figure 4a in which the correction has been applied "upwards" to a measured distribution showing how the inversion of the rotational population can be masked by predissociation. This effect is even more dramatic in OH($\upsilon' = 2$) and OD($\upsilon' = 3$); this is shown in Figure 4b for OH($\upsilon' = 2$) in which the correction has been applied "downwards" to a calculated distribution to determine the measured one to be expected. The drastic reduction of measured population that is predicted when the predissociation effect is taken into account is consistent with the very low populations observed for OH($\upsilon' = 2$) and OD($\upsilon' = 3$). In fact, the uncertainty in these measurements is such that applying the correction "upwards" does not produce reliable results. Consequently, the present study does not provide experimental rotational distributions for these levels.

The measured rotational distributions including the above predissociation correction are shown in Figures 5−7. In these figures, each rotational distribution is normalized to add up to unity. The main trend observed in the fragment rotational distributions consists of an increase of the population inversion with increasing excess excitation energy. The distributions for $\upsilon' = 0$ and 1 are strongly inverted and extend to N' values higher than N'_{max}, the highest energetically accessible rotational level. We attribute this effect to the initial thermal excitation of the parent molecule.[30] For both OH and OD, the distributions evolve smoothly with energy. At low excess energy, the distributions are rather flat with a slow falloff above N'_{max}. They become peaked toward N'_{max} as the excess excitation energy increases. When excitation of the ($\tilde{C}^1B_1 \leftarrow \tilde{X}^1A_1$) and ($\tilde{D}^1A_1 \leftarrow \tilde{X}^1A_1$) features takes place at wavelengths below 124 nm, the corresponding distributions fit smoothly in the trend.

Figures 5−7 also show the rotational distributions calculated using the DK and Leiden surfaces. Because these calculations take into account only the ground rotational level of the parent molecule, the distributions fall off at lower N' values than the corresponding experimental distributions. The calculations with both sets of surfaces follow the same general trend as the experiments, although the distributions obtained with the Leiden surfaces are in better agreement with the experimental results than those obtained with the DK surfaces. The population inversion for the DK surfaces appears much stronger than both the experiments and the Leiden surface calculations.

The population of each vibrational state is obtained, at each excitation wavelength, by summing up the populations of all rotational levels belonging to the vibrational state considered. When the predissociation correction is applied to retrieve the nascent populations for comparison with theoretical results, it should be kept in mind that the output of the TSVD procedure is a set of relative rovibrational populations that add up to unity. Therefore, care must be taken, after the predissociation corrections have been introduced, to renormalize the set of populations. As seen above, the OH($\upsilon' = 2$) and OD($\upsilon' = 3$) nascent populations cannot be experimentally determined. However, they are needed to properly normalize the set of vibrational populations, and therefore, they were approximated by the values supplied by the DK ab initio calculation. At 121.6 nm, the computed vibrational populations are very close to the ones found experimentally by Harich et al., lending further support to this approach.[45]

Figures 8 and 9 depict, as a function of the energy above threshold, the experimentally determined relative vibrational populations $P(\upsilon,E)$ for OH and OD, respectively. Results obtained here by synchrotron excitation are complemented by those obtained earlier by VUV laser excitation.[30] Ab initio results using the two sets of potential energy surfaces and statistical calculations are also compared in the figures with the present experiments. The ab initio vibrational populations rise sharply at threshold, and the experimental results show a similar behavior, although the rise is smoothened because of the significant rotation of the parent water molecules. It is seen that, contrary to what is found for the rotational distributions, the experimental vibrational distributions, for both OH and OD, are in better agreement with calculations using the DK ab initio surfaces. This would still be true if the Leiden results had been used to correct the experimental data for predissociation of OH(υ'=2) and OD(υ'=3).

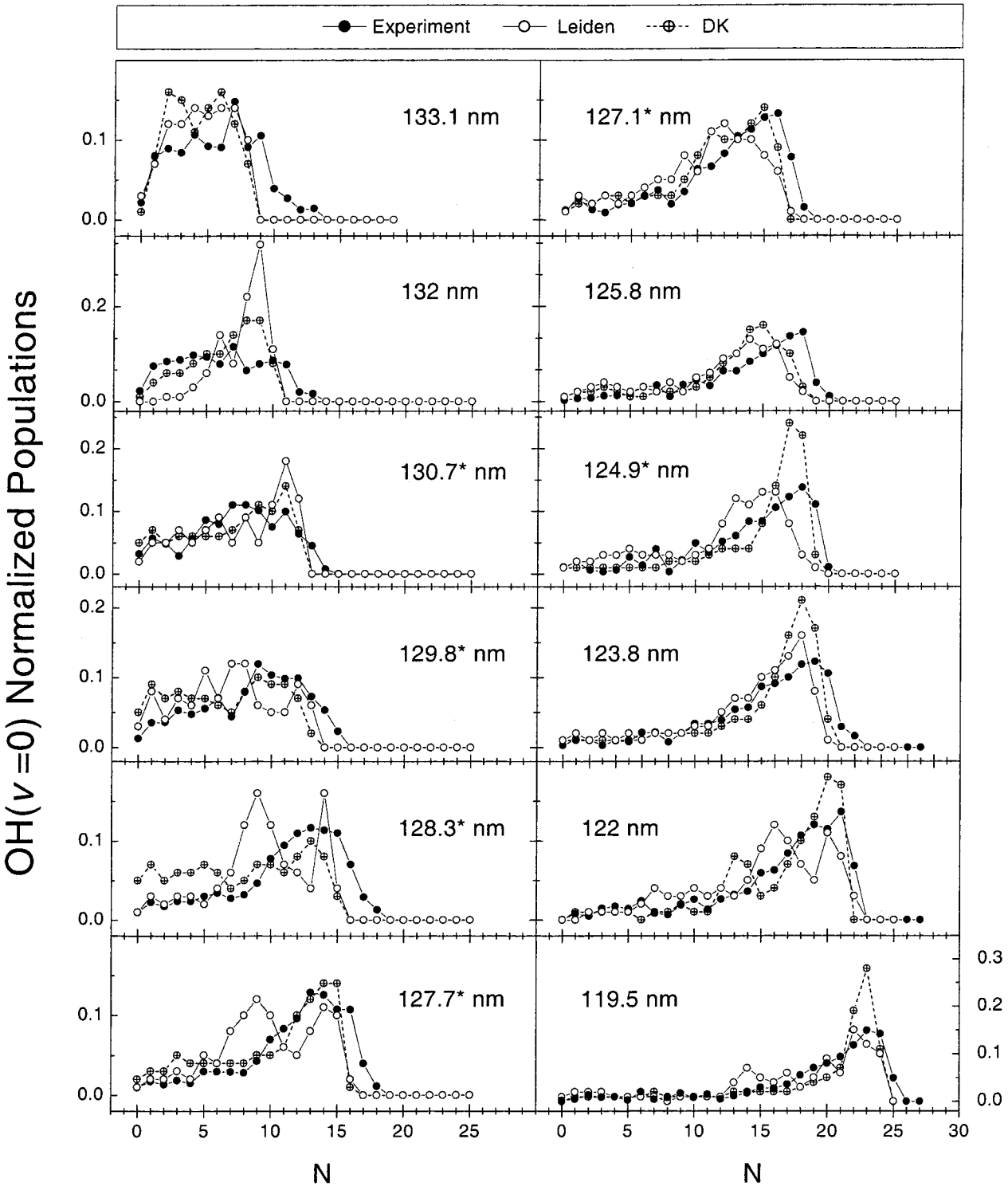

Figure 5. OH($A^2\Sigma^+, v' = 0$) rotational population distributions. The experimental values are compared to the quantum mechanical calculations using the Leiden and DK surfaces. Previous results obtained with VUV laser excitation[30] are indicated by an asterisk.

V. Discussion

Previous measurements and calculations of the internal energy distribution in the OH/OD(A) fragment following the photodissociation of the water molecule have generally been concerned mainly with the rotational degree of freedom. The present set of data, which includes both rotational and vibrational energy distributions, provides a good test of the quantum mechanical wave packet calculations on the two sets of three-dimensional PES considered in this work.

Most of the excitation wavelengths used in this experiment lead directly from the ground state to the excited $\tilde{B}$ state of the H_2O/D_2O molecule. At shorter wavelengths, as indicated in Table 1 (see also Figure 1), it is also possible to excite the first sharp Rydberg features of the spectrum corresponding to the $\tilde{C}(^1B_1)$ and $\tilde{D}(^1A_1)$ Rydberg states. However, in this case, it is expected that the dissociation dynamics should be completely determined by the evolution of the system on the $\tilde{B}$-state surface. Indeed, the initially excited $\tilde{C}$ and $\tilde{D}$ states are strongly coupled to the $\tilde{B}$ state, respectively, via Coriolis coupling[3,12] and by an

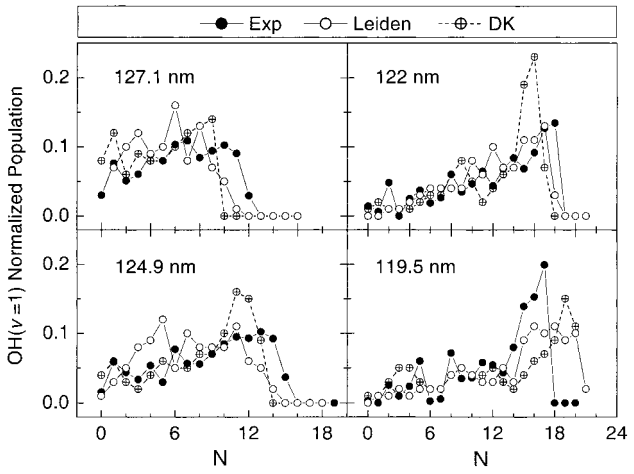

Figure 6. $OH(A^2\Sigma^+,\upsilon' = 1)$ rotational population distributions. The experimental values are compared to the quantum mechanical calculations using the Leiden and DK surfaces.

avoided crossing at bent geometries.[6,13] These couplings should provide a route for fast (picosecond) population transfer to the $\tilde{B}$ state, with little or no change in geometry, The $\tilde{B}$-state potential energy surface will subsequently control the evolution of the initial quantum mechanical wave packet. Thus, the present experiments are expected to provide information on the dissociation process initiated at any point of the $\tilde{B}$-state surface accessible from the ground state and provide a useful tool to probe the $\tilde{B}$-state surface even in regions where the $\tilde{B}-\tilde{X}$ Franck−Condon factors are not favorable.

The present set of experimental results is entirely compatible with this interpretation. Indeed, the measured rotational energy disposal in the OH/OD(A) fragments that follows resonant excitation of ($\tilde{C}^1B_1 \leftarrow \tilde{X}^1A_1$) and ($\tilde{D}^1A_1 \leftarrow \tilde{X}^1A_1$) transitions presents the same general trend as that found upon direct excitation to the $\tilde{B}$ state (Figures 4−6). Further support for this interpretation comes from the fact that the agreement between the rotational distributions obtained experimentally and those obtained by calculations that take into account only the $\tilde{B}$-state dynamics tends to be better, if anything, at higher energies even though Rydberg state excitations are involved. Although the dissociation process that takes place after excitation to the $\tilde{C}$ or $\tilde{D}$ states proceeds via the $\tilde{B}$-state surface, one could expect the bending and stretching modes initially excited in the parent water molecule to influence the rotation and vibration of the OH fragment, respectively. However, this does not seem to be taking place. Indeed, excitation of H_2O at 122.0 nm results in only about 20% of the absorption going into the $\tilde{C}(010)$ subband, which is expected to promote the bending motion of the parent molecule.[3] However, at this wavelength, the measured rotational distribution of OH does not show any increase of the photofragment rotational excitation. Moreover, no difference has been observed between OH(A) and OD(A) rotational distributions at 122.0 nm (121.9 nm for D_2O) despite the fact that the bending mode is excited in the first case and not in the second. However, one should not rule out the possibility that a small effect could be masked because of thermal averaging over a set of initial H_2O/D_2O rotational levels.

The experimentally determined probabilities, $P(\upsilon',E)$, of forming $OH/OD(A^2\Pi)$ fragments in the vibrational state, υ', as functions of the amount of excess energy, E (i.e., the energy available above the threshold for $OH(A,\upsilon'=0)$ production), are compared in Figures 8 and 9 with the present theoretical calculations using the Leiden[7] and DK[37] sets of potential energy surfaces. The theoretical $P(\upsilon',E)$ functions have been calculated for the lowest rotational level of the parent molecule, ($J'' = 0$,) and therefore do not take into account their initial rotational excitation. These functions rise quickly above the threshold in good agreement with the trend of the experimental results. However, this sharp rise is attenuated in the experimental data set because of the significant rotation of the parent water molecules at room temperature. Such behavior is expected for a statistical product state distribution when each open fragmentation channel has the same probability of being occupied. A statistical product state distribution is expected when the dissociating system follows indirect trajectories on the potential energy surface and the intermediate complex lives long enough to allow free energy distribution between the degrees of freedom. Statistical vibrational distributions, similar to the ones described in ref 30, calculated for $J'' = 0$ are also shown in Figures 8 and 9. They agree quite well, for both H_2O and D_2O, with the calculated vibrational distributions using the Leiden surfaces. The experimentally determined vibrational populations are significantly lower than both the Leiden and the statistical calculations. This is taken as an indication that the actual lifetime of the excited complex is not long enough for the vibrational population to be statistically distributed. On the other hand, the $P(\upsilon,E)$ functions calculated with the DK surfaces are in good agreement with the experimental data suggesting that the dynamics on the DK surfaces is more direct than that on the Leiden surfaces and provides a better picture of the experimental results. The small offsets observed on Figures 8 and 9 between the vibrational excitation thresholds correspond to the differences in the experimental and calculated OH and OD vibrational energies noted in section III and Table 2.

The measured and calculated rotational population distributions displayed in Figures 5−7, together with theoretical results for the Leiden and DK surfaces, show an increase of population inversion both with increasing energy and with decreasing vibrational quantum number. This behavior indicates that the population inversion is directly determined by the excitation excess energy. The population inversion is an indication of nonstatistical behavior. If the rotational distributions were determined statistically, then for $J'' = 0$, they would be independent of the rotational quantum number, j, of the fragment for all open j channels (for $J'' > 0$, the rotational distributions may show a weak j dependence for $j < J''$). Thus, not unexpectedly, it appears that the dynamics becomes more direct when the excess energy increases.

It has already been mentioned in the preceding section that, although the calculations with both Leiden and DK surfaces follow the same general trend as the experimental data, the population inversion for the DK surface is much stronger than that observed experimentally, while the population inversion for the Leiden surface is closer to the experiment. This agrees with the conclusion drawn in view of the vibrational distributions that the dynamics on the DK surface is more direct than that on the Leiden surface.

The differences between the DK and Leiden results can be attributed to the stronger excitation of symmetric stretch motions on the Leiden surface. This is related to the difference in the symmetric stretch potentials discussed before (see Figure 2). The initial stretching and bending motions of the parent molecule correlate asymptotically (at $R = \infty$) with the OH/OD(A) vibrational and rotational motions. Excitation of the symmetric stretch motion favors vibrational excitation of the OH/OD fragment resulting in a less direct dynamics on the Leiden surface. The corresponding dissociation process yields more

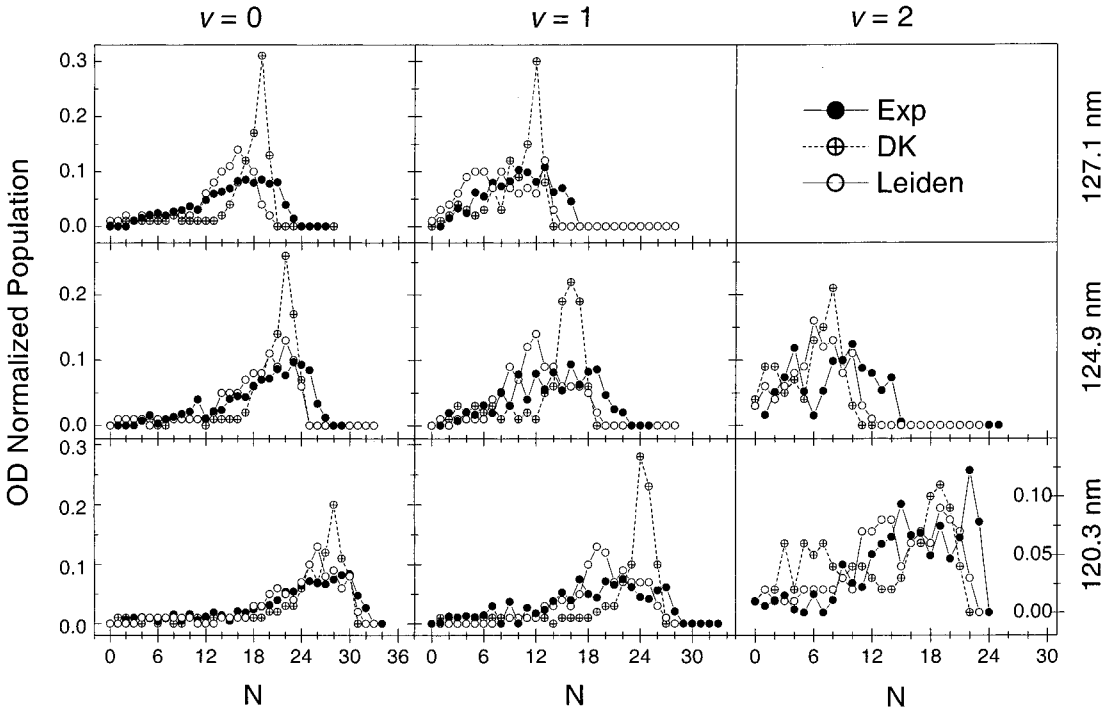

Figure 7. OD($A^2\Sigma^+,v' = 0, 1, 2$) rotational population distributions. The experimental values are compared to the quantum mechanical calculations using the Leiden and DK surfaces.

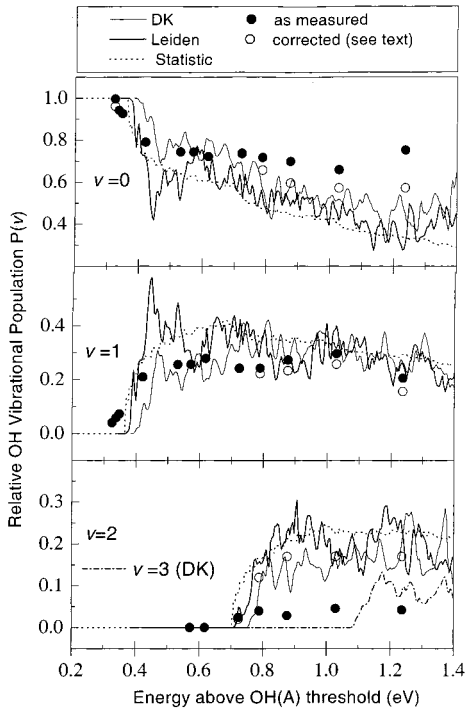

Figure 8. OH($A^2\Sigma^+,v'$) vibrational branching ratios vs excitation energy above the OH($A^2\Sigma^+,v' = 0$) threshold. Experimental values have been corrected for predissociation. Calculated values close to those obtained with the DK surface[37] have been used for $v' = 2$ (see text). The statistical results and dynamical calculations using the Leiden and DK surfaces are also shown. The small offsets observed between the excitation thresholds correspond to the differences in the experimental and calculated OH vibrational energies noted in section III and Table 2.

vibrationally excited OH/OD(A) fragments with weaker rotational population inversion due to a more statistical distribution of the energy over the degrees of freedom.

Thus, one particular feature of the potential energy surface, the symmetric stretch potential, is essential to explain the differences in both the vibrational and the rotational distributions. The paradoxical situation that the experimental vibrational distributions are better represented by the DK results while the experimental rotational distributions show a better agreement with the Leiden results is presumably explained by the effect of initial rotation of the H_2O/D_2O molecules for the room-temperature experiment. Recent experiments by the group of X. M. Yang[45] on a water beam with a temperature of 10 K at the Ly α wavelength (121.6 nm) show a rotational distribution that is more strongly inverted than that found here at the nearby wavelength of 122 nm. This indicates that there is indeed an effect of initial rotation of the molecules on population inversion. The rotational distribution obtained with the DK surface is more in accord with this cold beam result than the one obtained with the Leiden surface. A word of caution is in place: inspection of Figure 5 shows that the details of the rotational distribution are rather sensitive to the precise wavelength. It therefore remains desirable to perform experiments on cold beams at many more wavelengths.

VI. Summary and Conclusions

The internal energy distribution of the OH/OD fragments produced in the $A^2\Sigma^+$ excited state by photodissociation of H_2O through the $\tilde{B}$ state has been systematically studied, both experimentally and theoretically. Experimental results obtained in this work using synchrotron radiation excitation have been combined with those obtained previously with a VUV laser source providing a systematic exploration of all the regions of the H_2O/D_2O $\tilde{B}$ state accessible from the ground state. The present results confirm that only the $\tilde{B}$-state dynamics is involved, even when the primary excitation is mediated by absorption to other excited states, namely, the $\tilde{C}$ and $\tilde{D}$ Rydberg states. This follows from their strong coupling with the $\tilde{B}$ state, which ensures very fast population transfer to the $\tilde{B}$-state surface. Wave packet calculations of the dissociation process on the $\tilde{B}$-state

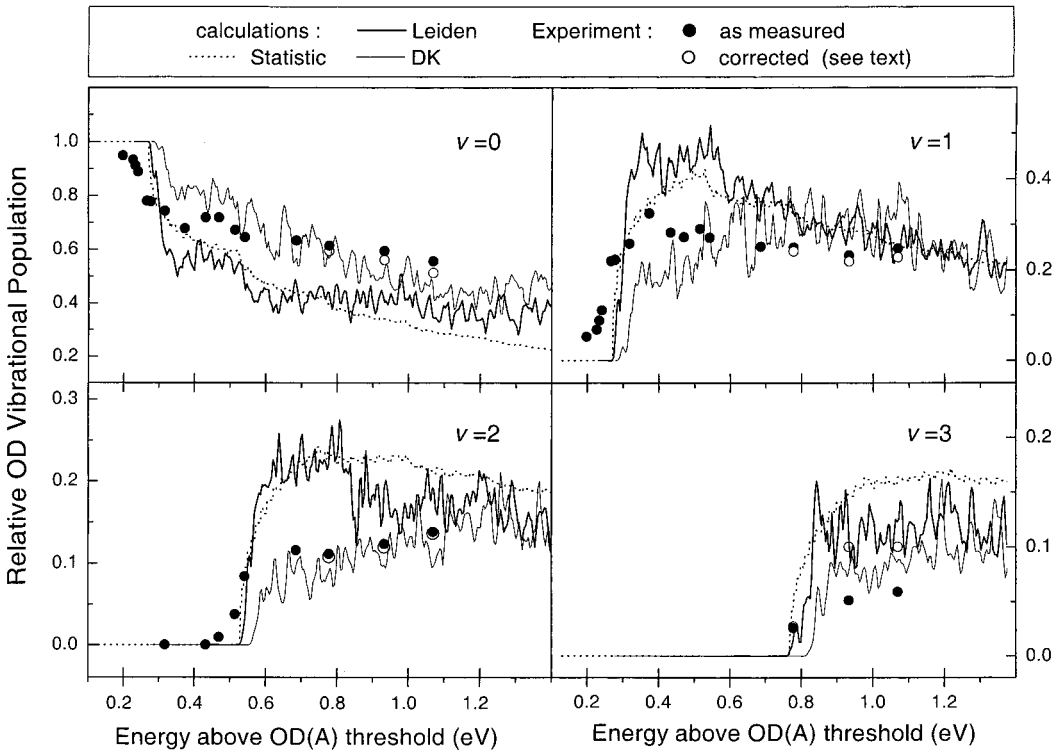

Figure 9. OD($A^2\Sigma^+$) vibrational branching ratios vs excitation energy above the OD($A^2\Sigma^+$,$v' = 0$) threshold. The $v' = 3$ values calculated with the DK surface[37] are used for the predissociation correction. The statistical results and dynamical calculations using the Leiden and DK surfaces are also shown. The small offsets observed between the excitation thresholds correspond to the differences in the experimental and calculated OD vibrational energies noted in section III and Table 2.

potential energy surface developed earlier[7] have been conducted here at the exact excitation energies that have been used in the experiments so that detailed comparisons could be made. The PES computed by the Leiden group[6] and that (as yet unpublished) obtained by Dobbyn and Knowles (DK)[37] have both been used in the calculations. A statistical calculation has also been made and used as a benchmark for comparison purposes.

Comparison of both wave packet and statistical calculations with the experimental results seems to indicate that the DK surface favors more direct dissociation trajectories than the Leiden one. This results from the fact that the former produces more strongly inverted rotational distributions and vibrational branching ratios that are more distant from the statistical result. This trend is attributed to the fact that the Leiden surface favors symmetric stretch vibrations, which tend to promote indirect trajectories and hence a more statistical behavior.

The experimental vibrational branching ratios are closer, at low excess excitation energy, to the DK results, while the rotational distributions are more akin to the softer profiles produced by the Leiden surface. It is felt that this could be due to the room-temperature Boltzmann distribution of the parent H_2O/D_2O molecules, which, if taken into account in the calculations, would result in less-peaked distributions. The DK distributions would thus come closer to the experimental ones, whereas the Leiden distributions would be pushed away.

At present, calculations including the thermal excitation of the H_2O rotational levels seem out of reach so that a desirable extension of the present work would be to run the experiments on a cool jet of water molecules. Hopefully, this would definitely validate the dynamics calculations and the DK potential energy surfaces.

Acknowledgment. R.v.H. and M.C.v.H. thank Professor Knowles for making available the DK potential prior to publication. The experiments were made possible thanks to adequate beam time allocation by LURE and support for travel expenses of J.R. and M.C. by the Large Installation Plan of the EU. This research benefited from a CNRS/CSIC exchange program and a visiting professorship granted to M.C. by Université de Cergy-Pontoise.

References and Notes

(1) Ashfold, M. N. R.; Langford, S. R. In *The Role of Rydberg States in Spectroscopy and Photochemistry*; Sándorfy, S., Ed.; Kluwer Academic: Dordrecht, The Netherlands, 1999.
(2) Child, M. S. *Philos. Trans. R. Soc. London* **1997**, *A355*, 1623.
(3) Bell, S. *J. Mol. Spectrosc*. **1965**, *16*, 205.
(4) Wang, H.-Z.; Felps, W. S.; McGlynn S. P. *J. Chem. Phys*. **1977**, *67*, 2614.
(5) Weide, K.; Schinke, R. *J. Chem. Phys*. **1989**, *90*, 7150.
(6) van Harrevelt, R.; van Hemert, M. C. *J. Chem. Phys*. **2000**, *112*, 5777.
(7) van Harrevelt, R.; van Hemert, M. C. *J. Chem. Phys*. **2000**, *112*, 5787.
(8) Dixon, R. N. *Mol. Phys*. **1985**, *54*, 333.
(9) Mordaunt, D. H.; Ashfold, M. N. R.; Dixon R. N. *J. Chem. Phys*. **1994**, *100*, 7360.
(10) Johns, J. W. C. *Can. J. Phys*. **1971**, *49*, 944.
(11) Watanabe, K.; Jursa, A. S. *J. Chem. Phys.* **1964**, *41*, 1650.
(12) Ashfold, M. N. R.; Bayley, J. M.; Dixon, R. N. *Chem. Phys*. **1984**, *84*, 35.
(13) Hirst, D. M.; Child, M. S. *Mol. Phys*. **1992**, *77*, 463.
(14) Ashfold, M. N. R.; Bayley, J. M.; Dixon, R. N. *Can. J. Phys*. **1984**, *62*, 1806.
(15) Smith, P. L.; Yoshino, K.; Griesinger, H. E.; Black, J. H. *Astrophys. J*. **1990**, *250*, 166.
(16) Docker, M. P.; Hodgson, A.; Simons, J. P. *Mol. Phys.* **1986**, *57*, 129.
(17) Carrington, T. *J. Chem. Phys.* **1964**, *41*, 2012.
(18) Okabe, H. *J. Chem. Phys*. **1980**, *72*, 6642.
(19) Gedanken, A. *J. Mol. Spectrosc*. **1980**, *82*, 246.
(20) Papagiannakopoulos, P.; Fotakis, C. *J. Phys. Chem*. **1985**, *89*, 3439.
(21) Simons, J. P.; Smith, A. J.; Dixon, R. N. *J. Chem. Soc., Faraday Trans*. **1984**, *80*, 1489.

(22) Hodgson, A.; Simons, J. P.; Ashfold, M. N. R.; Bayley, J. M.; Dixon, R. N. *Mol. Phys*. **1985**, *54*, 351.
(23) Shafizadeh, N.; Rostas, J.; Lemaire J. L.; Rostas, F. *Chem. Phys. Lett*. **1988**, *152*, 75.
(24) Briggs, R. G.; Halpern, J. B.; Hancock, G.; Shafizadeh, N.; Rostas, J.; Lemaire, J. L.; Rostas, F. *Chem. Phys. Lett*. **1989**, *156*, 363.
(25) Atkins, C. G.; Briggs, R. G.; Halpern, J. B.; Hancock, G. *Chem. Phys. Lett*. **1988**, *152*, 81.
(26) Harich, S. A.; Hwang, D. W. H.; Yang, X.; Lin, J. J. *J. Chem. Phys*. **2000**, *113*, 10073.
(27) Weide, K.; Schinke, R. *J. Chem. Phys*. **1987**, *87*, 4627.
(28) Heumann, B.; Kühl, K.; Weide, K.; Düren, R.; Hess, B.; Meier, U.; Peyerimhoff, S. D.; Schinke, R. *Chem. Phys. Lett*. **1990**, *166*, 385.
(29) Segev, E.; Shapiro, M. *J. Chem. Phys*. **1982**, *77*, 5604.
(30) Zanganeh, A. H.; Fillion, J. H.; Ruiz, J.; Castillejo, M.; Lemaire, J. L.; Shafizadeh, N.; Rostas, F. *J. Chem. Phys*. **2000**, *112*, 5660.
(31) Ruiz, J.; Martín, M. *Comput. Chem*. **1995**, *19*, 417.
(32) Eidelsberg, M.; Jolly, A.; Lemaire, J. L.; Tchang-Brillet, W.-Ü. L.; Breton, J.; Rostas, F. *Astron. Astrophys*. **1999**, *346*, 705.
(33) Balint-Kurti, G. G. *Chem. Phys*. **1981**, *6*, 137.
(34) Balint-Kurti, G. G.; Dixon R. N.; Marston, C. C. *J. Chem. Soc., Faraday Trans*. **1990**, *86*, 741.
(35) Petrongolo, C. *J. Chem. Phys*. **1988**, *8*, 1297.
(36) Dobbyn, A. J.; Knowles, P. J. *Mol. Phys*. **1997**, *91*, 1107.
(37) Dobbyn, A. J.; Knowles, P. J., to be submitted for publication.
(38) Murrell, J. N.; Carter, S.; Mills, I. M.; Guest, M. F. *Mol. Phys*. **1981**, *42*, 605.
(39) Coxon, J. A. *Can. J. Phys*. **1980**, *58*, 933.
(40) Clyne, M. A. A.; Coxon, J. A.; Woon Fat, A. R. *J. Mol. Spectrosc*. **1973**, *46*, 146.
(41) Yarkony, D. R. *J. Chem. Phys*. **1992**, *97*, 1838.
(42) Brzozowsky, J.; Erman, P.; Lyyra, M. *Phys. Scripta* **1978**, *17*, 507.
(43) Bergeman, T.; Erman, P.; Haratym Z.; Larsson, M. *Phys. Scr*. **1981**, *23*, 45.
(44) Lee, L. C.; Suto, M. *Chem. Phys*. **1986**, *6*, 161.
(45) Harich, S. A.; Hwang, D. W. H.; Yang, X. F.; Lin, J. J.; Yang, X. M.; Dixon, R. N. *J. Chem. Phys*. **2000**, *113*, 10073.